Interfacial layer assisted, forming free, and reliable bipolar resistive switching in solution processed $BiFeO_3$ thin films

Cite as: AIP Advances 10, 025110 (2020); doi: 10.1063/1.5134972
Submitted: 4 November 2019 • Accepted: 16 January 2020 •
Published Online: 6 February 2020

Chandni Kumari,[1,2] Ishan Varun,[3] Shree Prakash Tiwari,[3] and Ambesh Dixit[1,4,a)]

AFFILIATIONS

[1] Department of Physics, Indian Institute of Technology Jodhpur, Rajasthan 342037, India
[2] Department of Electronics and Communication Engineering, Graphic Era (Deemed to be University) Dehradun, Uttarakhand 248002, India
[3] Department of Electrical Engineering, Indian Institute of Technology Jodhpur, Rajasthan 342037, India
[4] Center for Solar Energy, Indian Institute of Technology Jodhpur, Rajasthan 342037, India

[a)] Author to whom correspondence should be addressed: ambesh@iitj.ac.in

ABSTRACT

$BiFeO_3$ based resistive random access memory (RRAM) devices are fabricated using a low-cost solution process to study the effect of an Al top electrode on switching behavior and reliability. Fabricated devices demonstrated bipolar switching characteristics with a moderate I_{on}/I_{off} ratio, set and reset voltages of ~−1.3 V and ~0.8 V, DC and AC endurance of more than 250 cycles and 7100 cycles, respectively, and a retention time of over 10^4 s, confirming the non-volatile resistive switching behavior. The ohmic and trap filled space charge limited conduction dominates the conduction mechanism in the devices at lower and higher voltages, respectively. Moreover, impedance spectroscopy measurements substantiate the presence of an AlO_x layer at the Al/$BiFeO_3$ interface resulting from the Al–O interaction at the junction, which is the possible rationale of reliable complementary switching in these RRAM devices. The switching mechanism is elucidated using the formation and rupture of the oxygen vacancy mediated filament, assisted by the participation of a thin AlO_x layer at the Al/BFO interface. The role of the thin AlO_x layer is explained by modeling of impedances.

© 2020 Author(s). All article content, except where otherwise noted, is licensed under a Creative Commons Attribution (CC BY) license (http://creativecommons.org/licenses/by/4.0/). https://doi.org/10.1063/1.5134972

INTRODUCTION

Memory devices are the crucial elements of electronic systems and have been previously developed as drum memories, capacitor memory, magnetic core memory, matrix core memory, magnetic cards/tapes, and flash memory.[1,2] As per the demand of the current electronic industry, non-volatile memory devices should possess characteristics such as being fast and scalable, a large retention time, and low power consumption together with low material and processing costs.[3] The limitations of scaling and slow speed in commonly used flash memory devices encouraged the development of fast and reliable memory devices, such as the magnetic RAM (MRAM),[4,5] phase change RAM (PCRAM),[6,7] ferroelectric RAM (FeRAM),[8,9] and resistive RAM (RRAM), which are being explored as probable alternatives to the existing flash memories.[1]

In recent years, the RRAMs have been extensively investigated to be used as an alternative to the existing non-volatile memories because of its fast response, high density, simple structure, lower power consumption, excellent compatibility with CMOS technology, and scalability.[10] The RRAM devices are composed of a facile metal–insulator–metal (MIM) architecture, where the data have been stored in multiple electrical resistance states, namely, low resistance states (LRSs) and high resistance states (HRSs). In unipolar RRAM devices, resistance states are independent of the applied bias polarity, whereas in the case of bipolar RRAM devices, states are bias polarity dependent.[10–12] Furthermore, the RRAM can be either analog or binary/digital in nature. A digital RRAM shows an abrupt

change from the LRS to HRS and vice versa for the reset and set states, respectively, whereas an analog RRAM will exhibit gradual change.[13] The generally accepted switching phenomenon in these devices is explained by various mechanisms such as the formation and rupture of filaments,[14,15] charge trapping and detrapping,[16] and Schottky barrier height modulation.[17] Among these, the filamentary switching is the most adequate in metal oxide based RRAM devices. The formation of the filament between the top electrode (TE) and bottom electrode (BE) leads to the LRS, while filament rupturing leads to the HRS. The filament is formed by the migration of either metal ions or oxygen vacancies across the active layer, namely, the conducting bridge RAM (CBRAM) and the valence change memory (VCM), respectively.[18–20] Numerous binary and ternary oxides such as nickel oxide (NiO),[21] aluminum oxide (AlO_x),[22] titanium dioxide (TiO_2),[23] hafnium oxide (HfO_2),[24] tin oxide (SnO_2),[25] zinc oxide (ZnO),[26] zirconium oxide (ZrO_2),[27] copper oxide (Cu_2O),[28] molybdenum oxide (MoO_x),[29] strontium titanate ($SrTiO_3$),[30] lead zirconium titanate (PZT),[31] and barium titanate (BTO)[32] and bismuth ferrites ($BiFeO_3$)[33,34] are explored for RRAM device applications. There are studies showing both unipolar and bipolar switching behaviors where different switching mechanisms are used to explain their RRAM characteristics.[10,35,36] However, there is no consensus on the type of switching and the respective switching mechanism as several explanations are provided to understand the observed RRAM characteristics.

$BiFeO_3$(BFO) is a multiferroic material with ferroelectricity and anti-ferromagnetism existing together at or above room temperature.[37] It exhibits a rhombohedral phase with the bandgap in the range of 2.3–2.6 eV.[38–40] The thin films of BFO are synthesized using various deposition techniques such as Pulsed Laser Deposition (PLD), sputtering, solution methods, and spin coating for RRAM applications.[10,35,36] Spin coating is a simple and cost-effective deposition technique allowing the easy fabrication of thin films. However, depositing BFO using spin coating is very challenging because of the appearance of secondary phases during processing or post-processing steps.[41] Earlier, we have reported a spin coated BFO based RRAM with silver as the top electrode (TE) and FTO as the bottom electrode (BE) and demonstrated the robustness of RRAM devices over a period of time.[42]

This type of switching mechanism depends on the difference between the top and bottom electrodes' work functions as the interface at the metal–insulator junction plays a crucial role in the switching phenomenon.[43–45] This motivated us to understand the switching characteristics and mechanism of the BFO RRAM with a different metal as the top electrode. Here, in this paper, we report solution processed Al/BFO/FTO based RRAM devices, where aluminum is acting as the TE and FTO as the BE. The devices showed forming free, bipolar, non-volatile, RRAM characteristics with excellent reliability and stability.

EXPERIMENT

The BFO films are synthesized using sol consisting of bismuth nitrate pentahydrate [$Bi(NO_3)_3.5H_2O$, 98%, Alfa Asser] and iron nitrate nonahydrate [$Fe(NO_3)_3.9H_2O$, 98%, Alfa Asser] base precursors in 2-Methoxyethanol (2-ME). Here, 1.6 g of bismuth nitrate pentahydrate and 1.22 g of iron nitrate nonahydrate are dissolved into 10 ml of 2-ME solution. The solution is stirred for three hours at 80 °C, followed by its room temperature aging for 24 h. Furthermore, FTO substrates are ultra-sonicated in acetone, isopropyl alcohol (IPA), and deionized water (DI) each for 15 min, prior to deposition. The aged BFO solution is used for spin-coating on the FTO substrate at 3000 rpm for 30 s. After each deposition, the substrate is preheated at 350 °C for five minutes. The process is repeated 2 times to get the desired thickness of ~70 nm. Finally, the deposited BFO film is heated at 450 °C for 3 h in the air.

The structural and microstructural characterizations are carried out using X-Ray diffraction (XRD), Scanning Electron Microscope (SEM), and Atomic Force Microscopy (AFM) measurements. The bandgap of the BFO thin film is measured using UV-vis absorption spectroscopy measurements. The vibrational characterization is carried out using Raman spectroscopy measurements at room temperature. Aluminum top contacts are deposited by thermal evaporation through a shadow mask with a circular opening diameter of ~500 μm for contact formation, with ~500 μm separation between them. The thickness of deposited contacts is about 200 nm. Electrical characterization of fabricated RRAM devices is carried out using a Keithley 4200 semiconductor characterization system (SCS), and impedance measurements are performed using a Metrohm (Autolab) system.

RESULTS AND DISCUSSION

Structural and microstructural

The structural information of synthesized BFO thin films is studied using a Bruker powder X-ray diffractometer with the Cu K_α (1.54 Å) radiation source in the 20°–65° 2θ range, operated at a voltage and current of 40 kV and 40 mA, respectively. The step size is kept constant at 0.02°/s. The XRD pattern of BFO/FTO is shown in Fig. 1(a), showing enhanced texturing along (104) with respect to other planar orientations. The XRD peaks can be marked to the perovskite BFO (ICDD No. 71-2494) without any signature of the secondary phase, supporting the synthesis of phase pure rhombohedral polycrystalline BFO thin films. The diffraction peaks for FTO substrates are marked for identification. The surface morphology of BFO/FTO films is shown in the inset of Fig. 1(a), where the SEM micrograph (top panel) is substantiating the uniform smooth surface without any granular variations. Furthermore, the surface

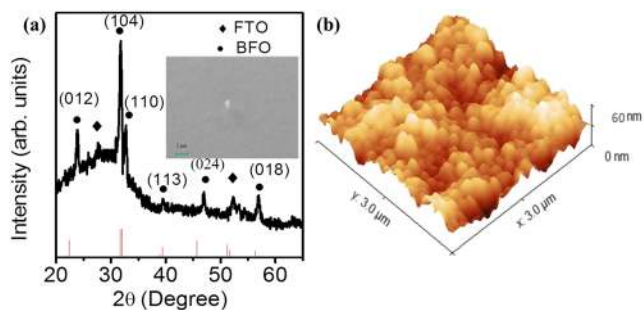

FIG. 1. (a) X-ray diffraction (XRD) pattern substantiating the impurity free rhombohedral phase with surface SEM (inset). The red lines correspond to the reference ICDD PDF No. 71-2494. (b) AFM micrographs indicating smoothness for BFO/FTO thin films.

© Author(s) 2020

topology and roughness of the film are analyzed using AFM measurements, Fig. 1(b). The calculated average and root mean square (rms) roughness of the film are 9.5 nm ± 2 nm and 9.16 nm ± 1.5 nm, respectively, substantiating SEM results for the deposited BFO/FTO thin films. The observed smooth surface with a lower rms roughness of deposited BFO/FTO thin films is important to realize the RRAM devices on these films.

Optical characterization

The absorption spectrum of BFO is measured using UV-vis spectroscopy measurement, as shown in the inset of Fig. 2(a). This is further used to calculate the bandgap using Tauc plot $(\alpha h\nu)^2$ vs energy hν, where h is Plank's constant, α is the absorption coefficient, and ν is the frequency, and is shown in Fig. 2(a) for BFO/FTO thin films. The bandgap is estimated using extrapolation as marked by a green straight line and is ~2.6 eV, Fig. 2(a), in agreement with the reported values.[38,42]

The vibrational analysis is carried out using room temperature Raman spectroscopy measurements. BFO crystalizes in a rhombohedral structure, consisting of two formula units in a single rhombohedral primitive unit cell. The factor group analysis at the gamma point (Γ) explains $\Gamma_{opt} = 4A_1 + 5A_2 + 9E$, where A_1 and E modes are longitudinal optical (LO) and transverse optical (TO) modes, respectively, and A_2 modes are Raman inactive. Thus, there are 18 phonon modes and only 13 modes are Raman active.[46–48] A_1(LO) and first/second order E(TO) modes represent contributions from Bi–O bonds. Third and fourth order E(TO) modes represent the contributions from Fe–O bonds. E(TO) substantiated the motion of atoms in "a" and "b" directions, and A_1(LO) substantiated the motion of atoms along the "c" direction.[47,48] We observed 2 A_1 modes which are A_1-1 and A_1-2 corresponding to 137 cm^{-1} and 168 cm^{-1} along with one E(TO) mode E_2 corresponding to 109 $cm,^{-1}$[47,48] which are observed in BFO thin films and are shown in Fig. 2(b), consistent with the reported literature.

Electrical characterization

For electrical characterization, the top electrode "TE" is subjected to applied voltage and the bottom electrode "BE" is kept at ground potential using a Keithley 4200 SCS. The applied bias is varied from −4 V → 0 V →3 V → 0 V → −4 V on the Al/BFO/FTO device. Device configuration is shown in the inset of Fig. 3(a). To protect the device from the permanent breakdown, a compliance current (CC) of 20 mA is applied during the measurement. This device is forming free, which is desirable as it will require lower operating voltages, thus leading to low power consumption. The device showed bipolar resistance switching with the set voltage on the negative side and the reset voltage on the positive side. The measured resistive memory current–voltage (I–V) curve is shown in Fig. 3(a), indicating the I_{on}/I_{off} ratio around one order of magnitude (~30) at −0.2 V. It is difficult to read the precise value of the set voltage; however, a substantial increase in current is visible around ~ −1.3 V and the device starts switching from a low current to the high current state. This brings the device from the HRS to LRS and is called the set process. The set is not abrupt but changing gradually for the Al/BFO/FTO RRAM device. The set voltage V_{set} is kept at ~−1.3 V. When a positive bias is applied, the current starts decreasing, and at ~0.9 V, the resistance starts changing from the LRS to HRS with reset voltage V_{reset} ~ 0.8 V. The reset process is also like the set process, exhibiting gradual changes. These polarity dependent set and reset processes substantiate bipolar resistive switching in Al/BFO/FTO RRAM devices. This gradual set and reset, which is taking place in the Al/BFO/FTO RRAM device, is also characterized as analog switching, thus showing the potential for neuromorphic memory applications.[13] The nonlinearity factor is defined as $I(V_{set})/I(0.5\ V_{set})$ and is ~5 for these RRAM devices.[49,50]

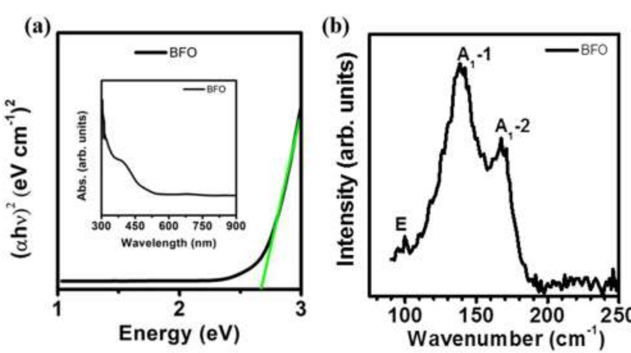

FIG. 2. (a) Tauc plot for BFO/FTO thins films with an inset showing the measured absorption spectra and (b) room temperature Raman spectra for BFO thin films.

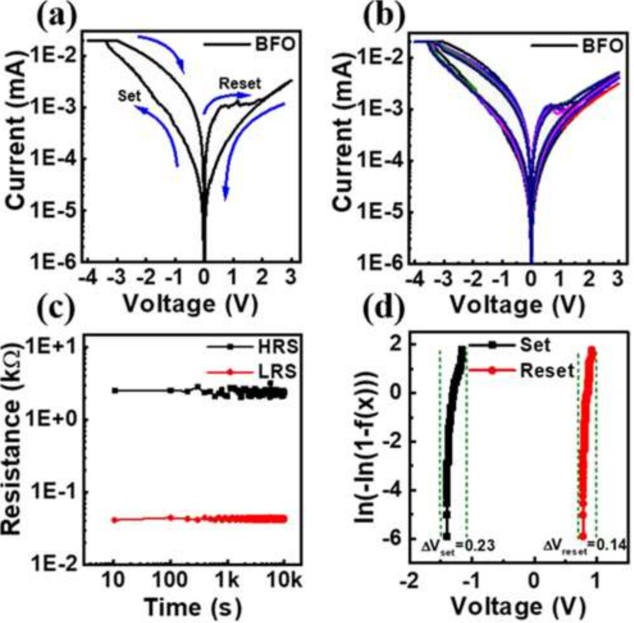

FIG. 3. Electrical characteristics of 500 μm × 500 μm Al/BFO/FTO RRAMs. (a) Single bipolar current–voltage characteristics curve with the device configuration shown in the inset, (b) multiple I–V curves for 250 cycles represented with different colors at an interval of 50 cycles, (c) retention curve for 10 000 s indicating non-volatility, and (d) Weibull's probability distribution curve for set and reset voltages substantiating the excellent reliability of Al/BFO/FTO RRAMs.

© Author(s) 2020

The devices showed reproducibility up to 256 cycles with a slight variation in the set and reset voltages, as shown in Fig. 3(b), showing multiple set/rest cycles. This result substantiates that the devices are stable and can work without any failure. The retention curve, Fig. 3(c), shows how long LRS and HRS windows are maintained without any significant degradation, supporting the stability of Al/BFO/FTO RRAM devices. The stability window is calculated for 10^4 s at 0.2 V in LRSs and HRSs. We can see that the window is maintained in the entire time span without any degradation. This result substantiates the non-volatility of Al/BFO/FTO RRAM devices.

The reliability of the device is analyzed using Weibull's distribution curve. Weibull's probability is expressed as $\ln[-\ln\{1-f(V)\}] = \beta \ln(V)$, where $f(V)$ is the set and reset voltage function and β is the shape parameter,[42] and is plotted in Fig. 3(d). The average V_{set} and V_{reset} values are −1.31 V and 0.78 V, respectively. The smaller variations in V_{set} (0.23 V) and V_{reset} (0.14 V) substantiate that the devices are highly reliable. The calculated shape parameter β is ~19 and 34 for V_{set} and V_{reset}, respectively. These higher values of β substantiate the uniform distribution of set and reset voltages. Furthermore, we plotted Weibull's distribution for the LRS and HRS at 0.2 V, Fig. 4(a). The LRS demonstrates almost constant resistance for consecutive cycles; however, a variation in HRSs is observed in the range of 3.5–6 kΩ. This fluctuation in HRSs is may be due to multiple filaments, which are not formed or ruptured during set and reset states. The average estimated values of the LRS and HRS are ~480 Ω and ~4.7 kΩ, respectively. The AC endurance of the devices is measured for 7100 AC pulses of 100 ms pulse width and is plotted in Fig. 4(b). The alternate set and reset voltages of −3 V and 1 V are applied to check the stability of devices, and it is noted that devices are able to switch on and off alternately with a smaller variation in ON and OFF currents.

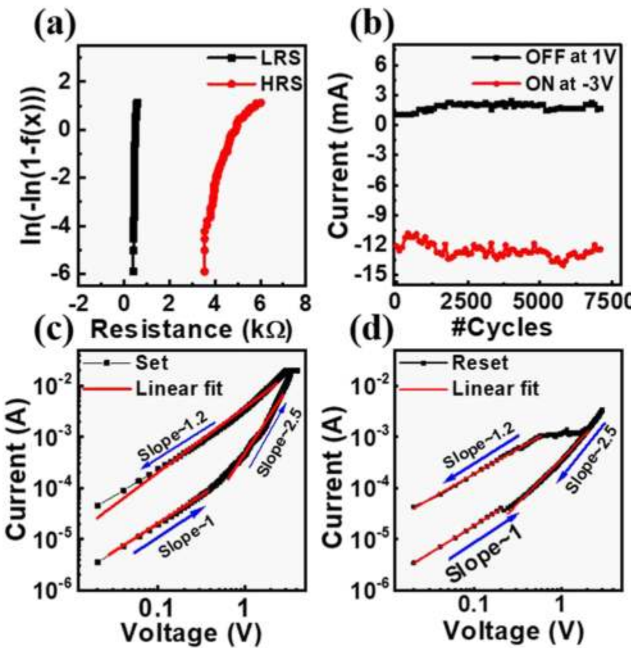

FIG. 4. (a) Weibull's distribution for LRSs and HRSs at 0.2 V, (b) AC endurance curve for 7100 cycles with ON and OFF voltages at −3 V and 1 V, substantiating the stability of the device, and log I–log V plots for the (c) set state and (d) reset state where Ohmic conduction is observed at lower voltages and SCLC at higher voltage regions of the HRS in Al/BFO/FTO RRAM devices.

The switching mechanism is investigated using the logarithmic current–voltage, i.e., log(I)–log (V), plots for LRSs and HRSs and is shown in Fig. 4(c). The HRS curve can be divided into two regions. In the first region, the slope of the graph is nearly 1 (i.e., I α V), substantiating the ohmic conduction mechanism in the lower voltage region, and the higher voltage range follows the I α $V^{2.5}$ power law, substantiating the trap-assisted space charge limited current (SCLC) conduction in a higher voltage window.

Thus, Ohmic conduction is responsible for the LRS, which signifies the filament formation inside the device. The different conduction mechanisms for the HRS and LRS substantiate that switching is taking place because of filament formation.[42] A similar type of conduction mechanism is observed for the reset state, Fig. 4(d). Initially the LRS is maintained, preserving the Ohmic conduction across the device. Furthermore, when the voltage is reduced, the filled defect states become empty and the device conducts due to low thermally generated current, reaching Ohmic behavior.

The filament formation can be due to the diffusion of metal ions or due to the presence of oxygen vacancies, and both are explained by the SCLC conduction mechanism.[42] Furthermore, interfaces in Al/BFO/FTO may play the important role in carrier transport.[49] We used aluminum as top and FTO as bottom contacts, and their work function values are about 4.28 eV and 4.4 eV, respectively. The FTO BE behaves as an oxygen vacancy reservoir, which supplies and stores oxygen vacancies during resistive switching.[51] Aluminum is an easily oxidizing material because of its lower Gibbs free energy of formation.[45] Hence, aluminum will react with oxygen present near the surface of BFO and, thus, assist in making a thin AlO_x layer at the Al/BFO interface. This increases the number of oxygen vacancies near the electrode/material interface.[52] This formation of an AlO_x thin layer leads to forming free RRAMs because of the enhanced oxygen vacancies. This interface contains a large number of oxygen ions, assimilated from the BFO thin film leading to a large slope. These observations infer that the bipolar switching mechanism can be attributed to the double reservoir model.[52]

Furthermore, we carried out impedance spectroscopy measurements on Al/BFO/FTO in the reset state to understand the presence of the AlO_x layer and its impact. The applied frequency range is 1–10^5 Hz without any DC bias voltage. The measured Cole–Cole plot, i.e., a graph between real and imaginary impedance components, is shown in Fig. 5(a) with the inset showing the equivalent circuit model, used for simulating the impedance data. The equivalent circuit consists of a parallel combination of resistance (R_2) and capacitance (C_2) in conjunction with two series resistances (R_0 and R_3). Here, R_2 and C_2 are representing a pure BFO film without any interfacial AlO_x layer in the reset state and R_0 and R_3 are representing the contact resistances. The real and imaginary parts of the impedance for the reset state without the AlO_x layer, reset state with the AlO_x layer, and set state are computed for complex impedances of these circuits, insets of Figs. 5(a)–5(c), as

© Author(s) 2020

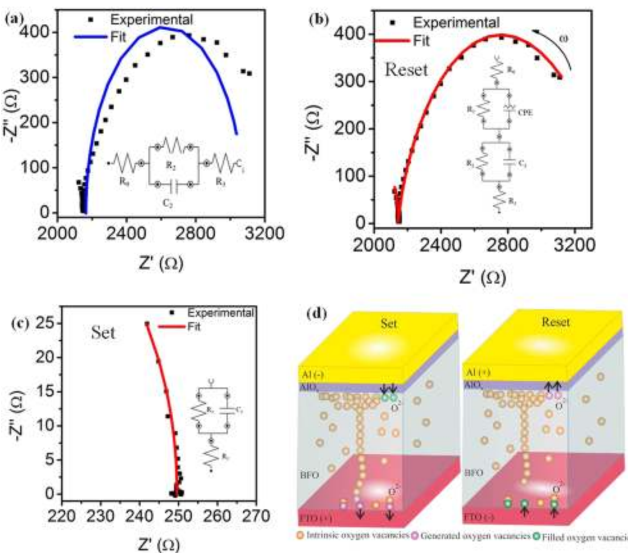

FIG. 5. (a) Impedance curve fitting of the HRS without considering the AlO_x layer with R_2 and C_2 representing the resistance and capacitance of the pure BFO thin film, respectively, (b) impedance curve fitting of reset with BFO and AlO_x layers, (c) impedance curve fitting of set, and (d) schematic of the AlO_x assisted filament formation mechanism for set and reset states in Al/BFO/FTO RRAM devices.

$$Z_{reset\ without\ AlOx} = \left[\frac{\left\{(R_0 + R_2 + R_3) + \omega^2\left(R_0R_2^2C_2^2 + R_2^2C_2^2R_3\right)\right\}}{1 + \omega^2R_2^2C_2^2}\right] + j\left[\frac{-\omega R_2^2C_2}{1 + \omega^2R_2^2C_2^2}\right], \quad (1)$$

$$Z_{reset\ with\ AlOx} = \left[\frac{\left\{(R_0 + R_2 + R_3) + \omega^2\left(R_0R_2^2C_2^2 + R_2^2C_2^2R_3\right)\right\}}{1 + \omega^2R_2^2C_2^2}\right] + j\left[\frac{-\omega R_2^2C_2}{1 + \omega^2R_2^2C_2^2}\right] + \left[\frac{R_1}{1 + j^n\omega^nQR_1}\right], \quad (2)$$

$$Z_{set} = \left[\frac{\left\{(R_1 + R_3) + \omega^2\left(R_1^2C_1^2R_3\right)\right\}}{1 + \omega^2R_1^2C_1^2}\right] + j\left[\frac{-\omega R_1^2C_1}{1 + \omega^2R_1^2C_1^2}\right]. \quad (3)$$

Here, Z is complex impedance $Z = Z' + jZ''$, with Z' as the real and Z'' as the imaginary impedance components, and ω is the angular frequency.

We observed that the fitting is not proper, Fig. 5(a) (solid blue line), substantiating that there is some additional contribution from another layer to the total impedance of the device. Furthermore, after introducing the interfacial layers in an equivalent circuit [the inset of Fig. 5(b)], consisting of an additional circuit element with resistance R_1 and a constant phase element (CPE), the impedance data are matching very well with the simulated (red solid line) impedance data, Fig. 5(b). The lower frequency region is attributed to the interface, and the higher frequency region is attributed to the BFO thin film. It is evident from the equivalent circuit that a parallel combination of resistance (R_1 = 1.2 kΩ) and constant phase element (CPE, n = 0.7) is essential in series along with a parallel combination of capacitance (C_2 = 728 pF) and resistance (R_2 = 800 Ω) for BFO thin films to fit the measured impedance data. The presence of this additional circuit element is attributed to the presence of a thin AlO_x layer at the interface of an Al top contact and a BFO thin film. The resistance of the AlO_x interface layer is higher than that of the BFO thin film, and the estimated resistivity value is ~4.7×10^4 Ω-m for an ~5 nm thick AlO_x layer. The estimated value is relatively lower than the resistivity value of pure alumina. This is attributed to the defects present in the AlO_x interface layer. Additionally, the resistivity of alumina decreases with increasing temperature and this may be another reason for the observed lower resistivity values as during the set process, the temperature inside the film will be relatively higher because of localized resistive losses. R_0 and R_3 resistances are contact resistances near the Al/AlO_x and FTO/BFO interfaces, and a combined value of ~1.7 kΩ is noted. The higher interface resistance near the FTO/BFO interface leads to the high set voltage requirement for oxygen ion exchange at the interface. CPE is a constant phase element, which is a complex element and is a combination of resistance and capacitance. The value of capacitance in the CPE is extracted as $C = (Q * R^{1-n})^{1/n}$, where Q is a CPE parameter; the CPE is a pure capacitor when n = 1 and a pure resistor when n = 0. The values of Q and n are independent of the frequency. We noted that n = 0.7 for the CPE, and its presence is attributed to heterogeneity or distributed elements present inside the AlO_x layer.[53]

The impedance curve for the set process is shown in Fig. 5(c), exhibiting a slightly tilted straight line with most of the points accumulated at the bottom. The equivalent circuit for the set process is given in the inset of Fig. 5(c). This confirms the filament formation inside the device. The equivalent circuit consists of a parallel combination of resistance (R_1 = 870 Ω) and capacitance (C_1 = 575 pF), attributed to the presence of an AlO_x layer. The CPE in the AlO_x layer, which was present during the reset state, is now replaced by a pure capacitor in the set state. This capacitor is present because of the formation of filaments from the FTO/BFO interface to AlO_x/BFO interface, which is not across the entire AlO_x surface. The resistance AlO_x layer is lower in the set state with respect to the reset state because of the oxygen ion migration in AlO_x during the set process. The series resistance (R_0 = 1.63 kΩ) is the combination of the filament resistance and contact resistances. The capacitance of BFO is replaced by a resistance because of the filament formation. The BFO resistance is ~250 Ω in the set state which is smaller with respect to that in the reset state, confirming the filament formation. Thus, we find that the contact resistances are nearly the same, whereas the bulk BFO resistance has changed significantly due to filament based conduction in the reset state.

The schematic diagram of the switching mechanism is shown in Fig. 5(d). The O^{2-} migrates from the AlO_x/BFO interface toward BFO after applying negative bias at the aluminum electrode and fills some oxygen vacancies. In addition, since the number of vacancies is much larger near the AlO_x/BFO interface, all the vacancies will not be filled and accumulation of oxygen vacancies will become a part of the electrode.[52,54–56] In addition, the negative bias will push the oxygen ions toward FTO. When oxygen ions move into FTO, oxygen vacancies will be created near the BFO/FTO interface. These generated oxygen vacancies will align from FTO toward the BFO/AlO_x interface and combine with the oxygen vacancies present near AlO_x. This will facilitate the filament formation of oxy-

© Author(s) 2020

TABLE I. Switching performance comparison of some recent reports on BFO based RRAMs. HT: Hydrothermal, SP: Solution processing, and PLD: Pulse laser deposition.

Device	Deposition method	Retention time (s)	I_{on}/I_{off} ratio	V_{set}/V_{reset} voltage	Endurance (Cycles)	Switching mechanism	References
Au/BFO/SRO	PLD	10^4	30		300	Oxygen vacancy migration	34
Pt/BFO/Pt	Sputtering	3000	10^4	1.5/−3.5	NA	Oxygen vacancy migration	10
Pt/BFO/NSTO	HT	2000	NA	2/−3	200	Carrier trapping–detrapping	55
Au/BFO/Pt	PLD	10^5	50		10^4	Schottky barrier	56
Ag/BFO/FTO	SP	10^4	450	1.1/−1.5	10^3	Metal ion filament	42
Au/BFO/Pt	PLD	10^5	100	−8/8	3×10^4	Carrier trapping–detrapping	35
Al/BFO/FTO	SP	10^4	~70	−1.3/0.8	7100	AlO_x assisted oxygen vacancy filament	This work

gen vacancies, resulting in a conducting path, and the device will switch from the HRS to LRS, bringing it to the set state. The migration of oxygen ions into FTO will require higher voltages, and that is why, a higher set voltage is observed in such devices.[52,54]

Furthermore, oxygen ions can be pushed into AlO_x by applying positive voltage at the top electrode. This will generate the oxygen vacancies near the AlO_x region but also push oxygen ions from FTO toward aluminum simultaneously. Few oxygen ions will fill the vacancies of the conducting path near FTO and hence will lead to the rupturing of the oxygen vacancy filament. This will bring the device to the reset state. The reset voltage is low because the oxygen ions near the FTO need a smaller amount of energy to fill the vacancies at the FTO/BFO interface.[52] A comparison of our work with other BFO based RRAM work is presented in Table I.

CONCLUSION

We report on solution processed Al/BFO/FTO based RRAM devices. These devices showed decent reproducibility and reliability for more than 250 cycles. The results substantiate one order for I_{on}/I_{off}, and the set and reset voltages are ~ −1.3 V and 0.8 V, respectively. The non-volatile nature of the device is confirmed by measuring retention for 10^4 s. The endurance robustness for 7100 cycles substantiates the stability of the devices. The SCLC and ohmic conduction mechanisms substantiate the formation and rupture of the filament in these RRAM devices. Furthermore, impedance analysis provided evidence of the presence of the AlO_x layer at the Al/BFO interface, and the switching mechanism is attributed to oxygen filament formation assisted by this AlO_x layer present at the metal–insulator interface.

ACKNOWLEDGMENTS

Ambesh Dixit acknowledges the financial assistance from the Department of Science and Technology, Government of India through Project No. INT/Mexico/P-20/2016 for this work.

REFERENCES

[1] T. C. Chang, K. C. Chang, T. M. Tsai, T. J. Chu, and S. M. Sze, Mater. Today **19**, 254 (2016).
[2] K.-C. Chang, T.-C. Chang, T.-M. Tsai, R. Zhang, Y.-C. Hung, Y.-E. Syu, Y.-F. Chang, M.-C. Chen, T.-J. Chu, H.-L. Chen, C.-H. Pan, C.-C. Shih, J.-C. Zheng, and S. M. Sze, Nanoscale Res. Lett. **10**, 120 (2015).
[3] Y. T. Li, S. B. Long, Q. Liu, H. B. Lü, S. Liu, and M. Liu, Chin. Sci. Bull. **56**, 3072 (2011).
[4] J.-G. Zhu, Y. Zheng, and G. A. Prinz, J. Appl. Phys. **87**, 6668 (2000).
[5] A. Ney, C. Pampuch, R. Koch, and K. H. Ploog, Nature **425**, 485 (2003).
[6] S. Raoux, A. K. König, H. Y. Cheng, D. Garbin, R. W. Cheek, J. L. Jordan-Sweet, and M. Wuttig, Phys. Status Solidi B **249**, 1999 (2012).
[7] A. Gyanathan and Y.-C. Yeo, J. Appl. Phys. **112**, 104504 (2012).
[8] H. Ishiwara, Curr. Appl. Phys. **12**, 603 (2012).
[9] T. Kojima, T. Sakai, T. Watanabe, H. Funakubo, K. Saito, and M. Osada, Appl. Phys. Lett. **80**, 2746 (2002).
[10] R. K. Katiyar, Y. Sharma, D. G. Barrionuevo Diestra, P. Misra, S. Kooriyattil, S. P. Pavunny, G. Morell, B. R. Weiner, J. F. Scott, and R. S. Katiyar, AIP Adv. **5**, 037109 (2015).
[11] L. Liu, S. Zhang, Y. Luo, G. Yuan, J. Liu, J. Yin, and Z. Liu, J. Appl. Phys. **111**, 104103 (2012).
[12] H.-Y. Chen, S. Brivio, C.-C. Chang, J. Frascaroli, T.-H. Hou, B. Hudec, M. Liu, H. Lv, G. Molas, J. Sohn, S. Spiga, V. M. Teja, E. Vianello, and H.-S. P. Wong, J. Electroceram. **39**, 21 (2017).
[13] T. Shi, R. Yang, and X. Guo, Solid State Ionics **296**, 114 (2016).
[14] M. Li, F. Zhuge, X. Zhu, K. Yin, J. Wang, Y. Liu, C. He, B. Chen, and R.-W. Li, Nanotechnology **21**, 425202 (2010).
[15] X. Zhu, F. Zhuge, M. Li, K. Yin, Y. Liu, Z. Zuo, B. Chen, and R.-W. Li, J. Phys. D: Appl. Phys. **44**, 415104 (2011).
[16] X. Zou, H. G. Ong, L. You, W. Chen, H. Ding, H. Funakubo, L. Chen, and J. Wang, AIP Adv. **2**, 032166 (2012).
[17] A. Q. Jiang, C. Wang, K. J. Jin, X. B. Liu, J. F. Scott, C. S. Hwang, T. A. Tang, H. Bin Lu, and G. Z. Yang, Adv. Mater. **23**, 1277 (2011).
[18] R. Waser and M. Aono, Nat. Mater. **6**, 833 (2007).
[19] J. J. Yang, D. B. Strukov, and D. R. Stewart, Nat. Nanotechnol. **8**, 13 (2013).
[20] U. Celano, *Metrology and Physical Mechanisms in New Generation Ionic Devices* (Springer International Publishing, Cham, 2016).
[21] D. Ielmini, F. Nardi, and C. Cagli, Nanotechnology **22**, 254022 (2011).
[22] J. Zhou, F. Cai, Q. Wang, B. Chen, S. Gaba, and W. D. Lu, IEEE Electron Device Lett. **37**, 404 (2016).
[23] D. S. Jeong, H. Schroeder, U. Breuer, and R. Waser, J. Appl. Phys. **104**, 123716 (2008).
[24] L. Zhao, S. Clima, B. Magyari-Köpe, M. Jurczak, and Y. Nishi, Appl. Phys. Lett. **107**, 013504 (2015).
[25] C. H. Nieh, M. L. Lu, T. M. Weng, and Y. F. Chen, Appl. Phys. Lett. **104**, 213501 (2014).
[26] X. Cao, X. Li, X. Gao, X. Liu, C. Yang, R. Yang, and P. Jin, J. Phys. D: Appl. Phys. **44**, 255104 (2011).
[27] S.-Y. Wang, D.-Y. Lee, T.-Y. Huang, J.-W. Wu, and T.-Y. Tseng, Nanotechnology **21**, 495201 (2010).
[28] L. D. V. Sangani, C. R. Kumar, and M. G. Krishna, J. Electron. Mater. **45**, 322 (2016).

© Author(s) 2020

[29] D. Lee, D. Seong, I. Jo, F. Xiang, R. Dong, S. Oh, and H. Hwang, Appl. Phys. Lett. **90**, 122104 (2007).
[30] Y. Watanabe, J. G. Bednorz, A. Bietsch, C. Gerber, D. Widmer, A. Beck, and S. J. Wind, Appl. Phys. Lett. **78**, 3738 (2001).
[31] H. Kohlstedt, A. Petraru, K. Szot, A. Rüdiger, P. Meuffels, H. Haselier, R. Waser, and V. Nagarajan, Appl. Phys. Lett. **92**, 062907 (2008).
[32] Z. Yan, Y. Guo, G. Zhang, and J. M. Liu, Adv. Mater. **23**, 1351 (2011).
[33] Y. Shuai, X. Ou, C. Wu, W. Zhang, S. Zhou, D. Bürger, H. Reuther, S. Slesazeck, T. Mikolajick, M. Helm, and H. Schmidt, J. Appl. Phys. **111**, 07D906 (2012).
[34] Y. B. Lin, Z. B. Yan, X. B. Lu, Z. X. Lu, M. Zeng, Y. Chen, X. S. Gao, J. G. Wan, J. Y. Dai, and J.-M. Liu, Appl. Phys. Lett. **104**, 143503 (2014).
[35] T. You, N. Du, S. Slesazeck, T. Mikolajick, G. Li, D. Bürger, I. Skorupa, H. Stöcker, B. Abendroth, A. Beyer, K. Volz, O. G. Schmidt, and H. Schmidt, ACS Appl. Mater. Interfaces **6**, 19758 (2014).
[36] K. Bogle, R. Narwade, A. Phatangare, S. Dahiwale, M. Mahabole, and R. Khairnar, Phys. Status Solidi A **213**, 2183 (2016).
[37] N. A. Spaldin, S. Cheong, and R. Ramesh, Phys. Today **63**(10), 38 (2010).
[38] J. F. Ihlefeld, N. J. Podraza, Z. K. Liu, R. C. Rai, X. Xu, T. Heeg, Y. B. Chen, J. Li, R. W. Collins, J. L. Musfeldt, X. Q. Pan, J. Schubert, R. Ramesh, and D. G. Schlom, Appl. Phys. Lett. **92**, 142908 (2008).
[39] P. S. V. Mocherla, C. Karthik, R. Ubic, M. S. Ramachandra Rao, and C. Sudakar, Appl. Phys. Lett. **103**, 022910 (2013).
[40] D. Sando, C. Carrétéro, M. N. Grisolia, A. Barthélémy, V. Nagarajan, and M. Bibes, Adv. Opt. Mater. **6**, 1700836 (2018).
[41] Q. Zhang, D. Sando, and V. Nagarajan, J. Mater. Chem. C **4**, 4092 (2016).
[42] C. Kumari, I. Varun, S. Prakash Tiwari, and A. Dixit, Superlattices Microstruct. **120**, 67 (2018).
[43] K.-L. Lin, T.-H. Hou, J. Shieh, J.-H. Lin, C.-T. Chou, and Y.-J. Lee, J. Appl. Phys. **109**, 084104 (2011).
[44] K.-J. Lee, L.-W. Wang, T.-K. Chiang, and Y.-H. Wang, Materials **8**, 7191 (2015).
[45] H. Young Jeong, S. Kyu Kim, J. Yong Lee, and S.-Y. Choi, J. Electrochem. Soc. **158**, H979 (2011).
[46] H. M. Hashem and M. H. Hamed, Mater. Chem. Phys. **211**, 445 (2018).
[47] S. Gupta, M. Tomar, V. Gupta, A. R. James, M. Pal, R. Guo, and A. Bhalla, J. Appl. Phys. **115**, 234105 (2014).
[48] M. Muneeswaran, P. Jegatheesan, M. Gopiraman, I.-S. Kim, and N. V. Giridharan, Appl. Phys. A **114**, 853 (2014).
[49] X.-C. Yuan, X.-H. Wei, B. Dai, and H.-Z. Zeng, Appl. Surf. Sci. **362**, 506 (2016).
[50] S. Kim, Y. F. Chang, and B. G. Park, RSC Adv. **7**, 17882 (2017).
[51] T. Shi, X. B. Yin, R. Yang, and X. Guo, Phys. Chem. Chem. Phys. **18**, 9338 (2016).
[52] K. K. Chiang, J. S. Chen, and J. J. Wu, ACS Appl. Mater. Interfaces **4**, 4237 (2012).
[53] H. Cesiulis, N. Tsyntsaru, A. Ramanavicius, and G. Ragoisha, *Nanostructures and Thin Films for Multifunctional Applications* (Springer International Publishing, Cham, 2016).
[54] A. Kumar, M. Das, V. Garg, B. S. Sengar, M. T. Htay, S. Kumar, A. Kranti, and S. Mukherjee, Appl. Phys. Lett. **110**, 253509 (2017).
[55] C. Gao, F. Lv, P. Zhang, C. Zhang, S. Zhang, C. Dong, Y. Gou, C. Jiang, and D. Xue, J. Alloys Compd. **649**, 694 (2015).
[56] T. You, X. Ou, G. Niu, F. Bärwolf, G. Li, N. Du, D. Bürger, I. Skorupa, Q. Jia, W. Yu, X. Wang, O. G. Schmidt, and H. Schmidt, Sci. Rep. **5**, 18623 (2015).

© Author(s) 2020